Bending behavior of cement-based multi-layered roof elements

Giulio Zani*, Marco Carlo Rampini, Matteo Colombo, Marco di Prisco

Politecnico di Milano, Department of Civil and Environmental Engineering, Piazza Leonardo da Vinci 32, 20133 Milano, Italy

ABSTRACT

The two major earthquakes occurred in Northern Italy in 2012 (magnitude 6.1 and 5.8) shown that a serious debate over the structural safety of existing industrial buildings is utterly necessary, also in regions traditionally considered less exposed to the seismic hazard. A promising retrofitting strategy may be represented by the substitution of inefficient secondary roof components with innovative lightweight panels, capable of simulta-neously ensuring a global reduction of the inertial forces and an increase of the building energy performances. In this paper, the structural behavior of a multilayered solution, consisting of an advanced cement-based case enclosing a thick insulating core, is presented and investigated on real-scale specimens. The mechanical char-acterization of the employed materials (High-Performance Fiber Reinforced Cementitious Composite and Textile Reinforced Concrete) at the laboratory level is followed by the discussion of the major challenges arisen in transferring such sensitive construction technologies to the prototyping plant. Structural performances are evaluated by means of longitudinal and transverse bending tests and simplified plane-section design approaches are finally explored and critically assessed.

Keywords:
High performance fiber reinforced cementitious composite
Textile reinforced concrete Sandwich panel
Lightweight roof element Bending behavior
Full-scale test
Plane-section analysis

1. Introduction

According to recent surveys, Italy is the second largest country in the European Union for the number of industrial buildings, counting about 650,000 structures, of which more than 120,000 only in the Lombardy Region [1]. A great part of them appears not to be longer in compliance with updated regulations, being characterized by unsatisfactory structural and energy performances. Given this context, a promising solution to limit soil consumption and effectively increase the overall quality of the industrial stock is represented by the replacement of existing cement-based roofing systems, frequently devoid of insulation layers, combined with hazardous asbestos components and vitiated by their significant self-weight (about 2–3 kN/m^2). In the aftermath of the launch of regional funding and national retrofitting incentives programs, Politecnico di Milano was involved in a research consortium committed to develop a sustainable cement-based secondary roof element characterized by lightness, structural safety, thermal efficiency and compatibility with photovoltaic devices. The proposed 2.5 × 5 m^2 panel is comprehensively displayed in Fig. 1; it consists of a multilayered structure, in which the internal insulating core is encased in thin high-performance cementitious composites. The cross-section represents the holistic synthesis of preliminary investigations aimed at meeting a series of target performances. The proposed solution is characterized by: (i) a self-weight of 1.2 kN/m^2; (ii) a thermal transmittance (average value accounting for the presence of thermal bridges) of 0.42 W/(m^2·K); (iii) a fire classification R30; (iv) the simple installation of building-integrated photovoltaic (PV) panels through glued connections and (v) water-tightness without additional membranes.

The structural concept harks back to the traditional sandwich technology [2], in which the outer wythes are coupled by means of a soft core and a significant bearing capacity is obtained thanks to the high bending stiffness to weight ratio [3–10]. At the meso-scale level, the mechanical transfer between the 20 mm thick High-Performance Fiber Reinforced Cementitious Composite (HPFRCC) [11,12] and the 10 mm thick Textile Reinforced Concrete (TRC) [13–16], reinforced with Alkali-Resistant (AR) glass fabrics, is entrusted to the core; in this sense, the polystyrene (EPS) is employed as a structural material, due to its capability to sustain weak, yet not negligible, shear stresses [3,5]. Two HPFRCC ribs reinforced with Φ14 mm ordinary steel bars run in the longitudinal direction. To favor a box-like behavior, the short sides are completed by 20 mm thick HPFRCC head plates, with the exception of the corner areas, where 100 mm thick blocks are introduced to adequately house anchoring and uplifting devices. Ductility and ro-bustness are finally enhanced by three additional fabric sheets, placed beneath the HPFRCC layers. The experimental campaign comprised

---

* Corresponding author.
E-mail addresses: giulio.zani@polimi.it (G. Zani), marcocarlo.rampini@polimi.it (M.C. Rampini), matteo.colombo@polimi.it (M. Colombo), marco.diprisco@polimi.it (M. di Prisco).

Published Journal Article available at: https://doi.org/10.1016/j.engstruct.2019.03.085

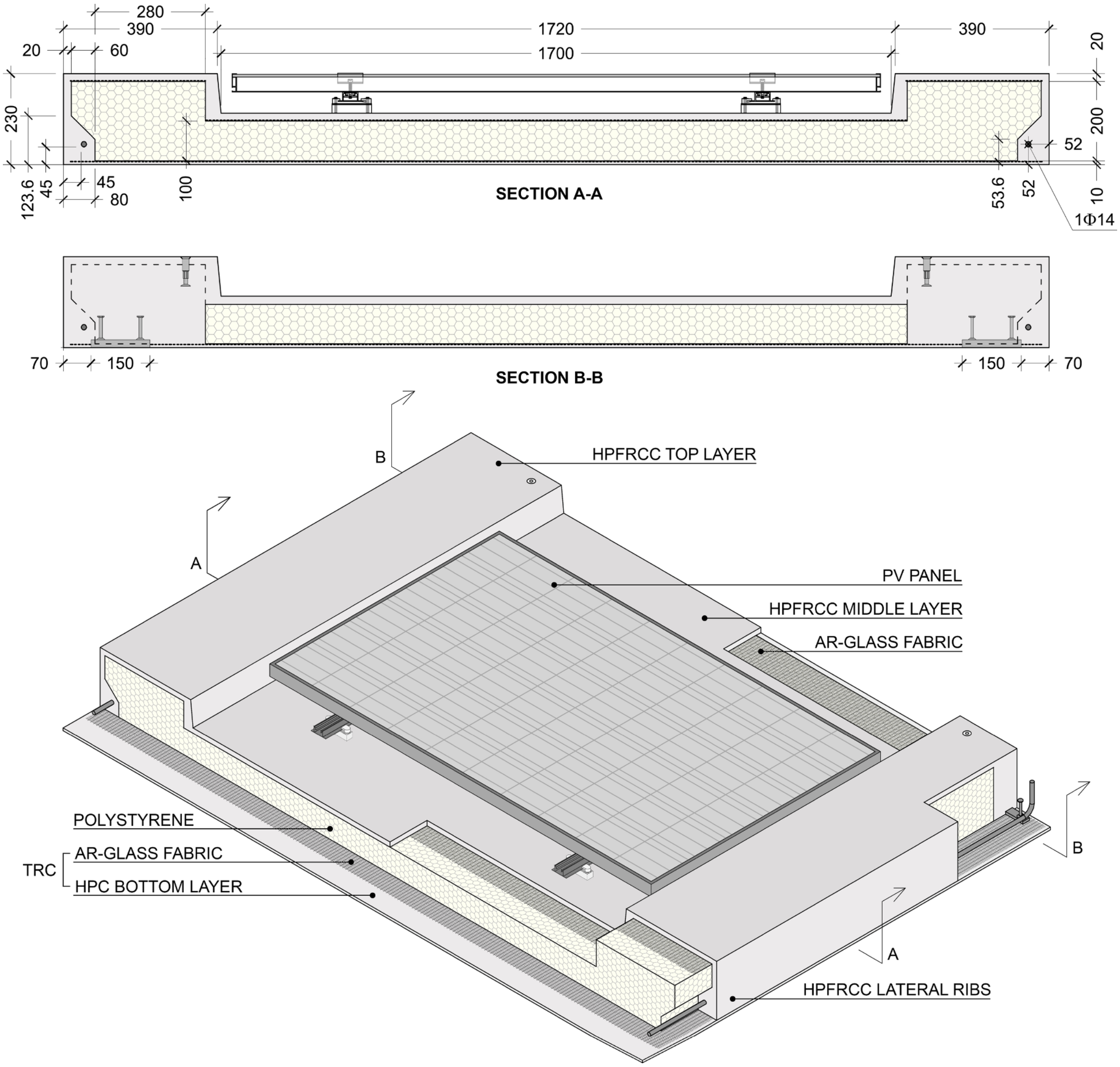

Fig. 1. Transverse sections and axonometric view of the proposed roofing panel (measures expressed in mm).

materials characterization, meso-scale investigations and full-scale tests, carried out on ten prototypes produced in a precast plant. Regarding the prototypes, two were tested in longitudinal bending, two in transverse bending, two in shear, one in fire conditions [17] and three were installed on a small demo-building to investigate on-field assembly operations, energy performances and durability in real environmental conditions [18]. In this paper, the experiments at the material level, aimed at defining the basic properties and provide effective constitutive laws, will be followed by the longitudinal and transverse bending responses and by simplified plane-section analyses proposing valuable structural design tools.

2. Materials

As mentioned, the panel consists of a thin-walled cementitious case enveloping a thick soft core. To control the overall weight, high-performance cement-based materials were employed, so as to decrease their thickness to minimum practical values. A 10 mm thick TRC was placed on the bottom tensile side, while a 20 mm thick HPFRCC was chosen for the remaining layers, following structural and fire considerations.

It is important to mention that, despite the middle and top HPFRCC layers were additionally reinforced with AR glass fabrics, they will not be referred in the following as hybrid composites, since the samples extracted from one nominally identical prototype (panel subjected to fire test, not discussed in this paper, Fig. 2) shown that a full embedment of the textiles within the matrix was achieved only in the bottom layer, thanks to the small thickness and the greater hydrostatic pressure exerted by the fresh-state concrete.

Each lateral rib was reinforced with a Φ14 mm B450C grade steel bar; uniaxial tensile tests, carried out according to the ISO 15630-1 Standard [19] on three nominally identical specimens, led to the following average properties: yield strength $f_y = 529.3$ MPa, ultimate strength $f_{su} = 611.3$ MPa and ultimate strain $\varepsilon_{su} = 10.8\%$ (in the analytical calculations an elastic modulus E_s of 210 GPa was also considered).

Regarding the core, even though different insulating materials and interlayer couplings were investigated at the meso-scale [20], an ordinary EPS 100, connected to the fresh-state cementitious materials by means of simple chemo-mechanical adhesion, was selected for its thermal properties, lightness, cheapness and mechanical ductility in shear. Due to the scarce relevance of the soft layer in the proposed analytical approach based on a plane-section kinematical model, its characterization will be omitted in the following. A comprehensive experimental investigation carried out on an analogous material can be found in [21].

(a) (b)

Fig. 2. Samples of the middle HPFRCC (a) and the bottom TRC (b) layers extracted from the full-scale panel.

2.1. HPFRCC

Preliminary design was based on a reference HPFRCC (Table 1); this first material was prepared at the laboratory scale, paying great attention to the water control, also in respect of the aggregates moisture contents. The mechanical responses of three nominally identical EN 14651 [22] notched beam specimens, encoded as Rilem Beams (RB) and tested under a center-point loading (RB in Fig. 3), are displayed in Fig. 4(a) (Reference RB and dark gray solid hatches). As one should note, the carefulness observed in the production resulted in remarkable residual stresses – f_{R1} and f_{R3}, respectively associated to Crack Mouth Opening Displacements (CMOD) typical of Serviceability ($\mathrm{CMOD}_1 = 0.5$ mm) and Ultimate ($\mathrm{CMOD}_3 = 2.5$ mm) Limit States – and limited coefficients of variation (Table 3); according to the *fib* Model Code 2010 (MC2010) [23,24], this material is classified as a 14a class fiber-reinforced composite (FRC).

The technology transfer at the industrial scale entailed a moderate adjustment of the original mix design, as it can be noticed in Table 2; in particular, the water dosage was increased, to ensure an effective transportation of the mix throughout the automated distribution line, and the reference straight high-carbon steel microfibers (length $l_f = 13$ mm, diameter $d_f = 0.16$ mm, aspect ratio $l_f/d_f \approx 80$) were substituted by the most similar product (in terms of shape and material strength) readily available on the market ($l_f = 13$ mm, $d_f = 0.20$ mm, $l_f/d_f = 65$).

In literature it is well known that the most critical issues concerning high performance self-compacting and self-leveling concretes are connected to their fresh-state conditions, with reference to the workability and the robustness exhibited in the casting phase. Since traditional concrete plants are designed to meet the quality requirements of ordinary cement-based admixtures, problems arise when sensitive composites such as HPFRCC are considered. In particular, the poor control of aggregates storage conditions, the need to extend workability and the excessive tolerances of humidity sensors might lead to an unsatisfactory control over the water content. This appears clear in Fig. 4(a) (Used RB), where the responses of ten nominally identical notched beams, produced together with the prototypes and tested after 28 days of natural curing, are displayed. As one should note, the specimens exhibited significant differences in their mechanical behavior due to the matrix lack of consistency which, in turn, caused a non-homogeneous fiber dispersion. Segregation phenomena occurred at two different stages: within the fresh-state concrete mixing and distribution apparatuses and, after the casting, within the specimen depth, as proved by the two cross-sections displayed in Fig. 4(a), showing uneven volume fractions and accumulation towards the bottom face of the molds. Although some curves appear to be close to the average reference behavior, the presence of significantly under-reinforced samples leads to a 3b classification, again based on the characteristic values of lognormal residual strength distributions (Fig. 4(b) and Table 3).

Table 1
Mix design of the reference HPFRCC (w/c = 0.33, w/b = 0.18).

Component	Dosage
Cement I 52.5	582 kg/m^3
Sand 0–2 mm	948 kg/m^3
Water	194 l/m^3
Superplasticizer	32 kg/m^3
Blast furnace slag	485 kg/m^3
Steel fibers $l_f/d_f = 13/0.16$	97 kg/m^3

It is worth noting that also the change in the fibers dimension might have played a substantial contribution to the overall material response: given the dosages of Tables 1 and 2, the choice of a greater wire dia-meter implied a 34% reduction of the number of fibers ($\propto d_f^2$), which penalizing effects were only partially balanced by the increase of the pull-out strength ($\propto d_f$).

In case of applications comprising markedly deflection-hardening materials or sections thinner than 150 mm subjected to bending, it is advantageous to perform a characterization on *structural* specimens (SB in Fig. 3). The mechanical response of five nominally identical 20 mm thick unnotched beam specimens, encoded as Structural Beams (SB), is displayed in Fig. 4(c), in terms of Nominal Stress vs. an integral Crack Opening Displacement (COD) measured over a 200 mm gage length. Third-point tests on thin unnotched samples highlighted significant differences in terms of sectional ductility, peak strength and toughness, thanks to the ability to account for the reduced thickness, the wall effects and the impact of the casting direction on fiber orientation [25].

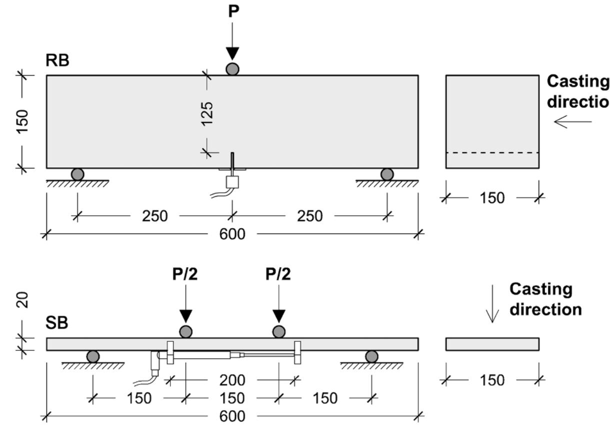

Fig. 3. Rilem beam (RB) specimen (top) and *structural* beam (SB) specimen (bottom) test configurations (measures expressed in mm).

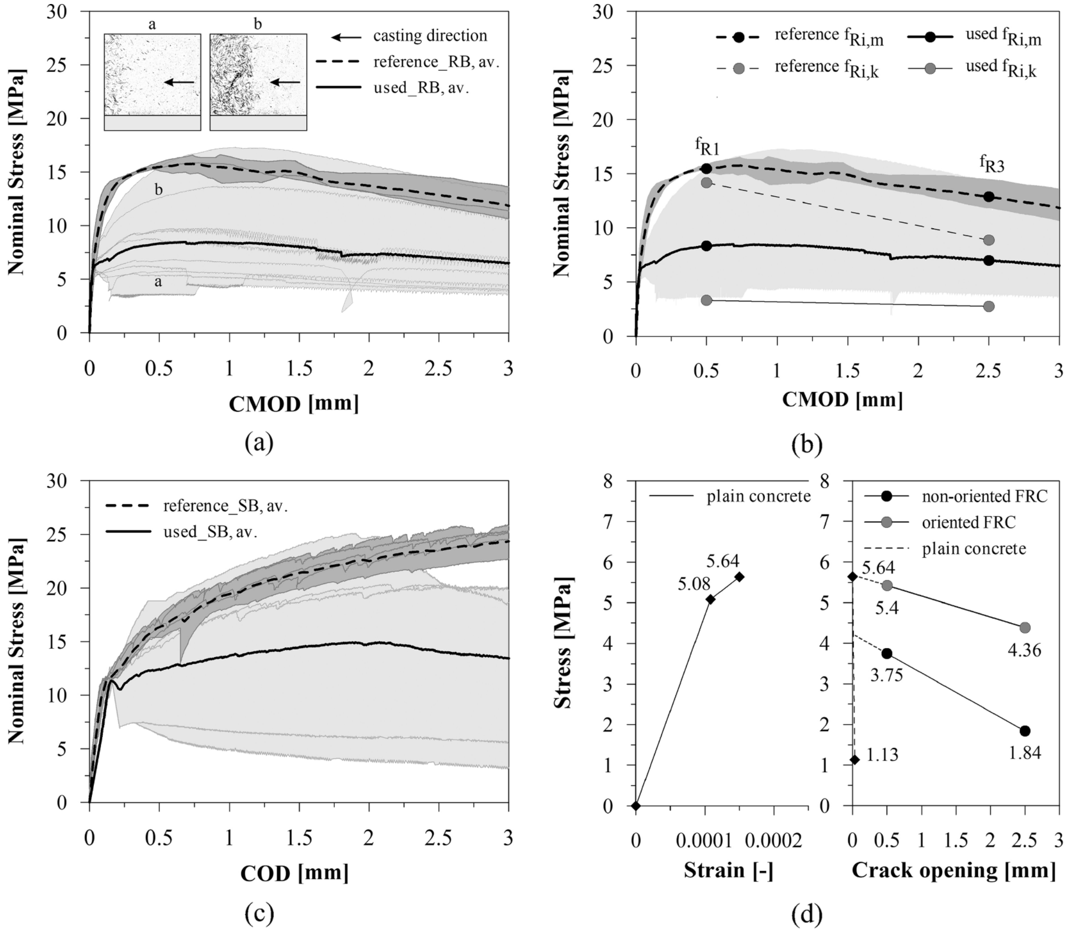

Fig. 4. HPFRCC material characterization: notched beams nominal stress vs. CMOD diagrams, together with two typical cross-sections (a), identification of notched beams average and characteristic residual strengths (b), *structural* beams nominal stress vs. COD diagrams (c) and identification of multilinear tensile laws (d).

Table 2
Mix design of the used HPFRCC (w/c = 0.38, w/b = 0.20).

Component	Dosage
Cement I 52.5	600 kg/m^3
Sand 0–2 mm	847 kg/m^3
Water	225 l/m^3
Superplasticizer	28 kg/m^3
Blast furnace slag	500 kg/m^3
Steel fibers l_f/d_f = 13/0.20	100 kg/m^3

By the comparison with the reference specimens, it is clear that despite fiber segregation within the depth is generally connected to better SB behaviors – due to a local increase of volume fraction on the tensile side (see the casting direction of Fig. 3) – the set generally resulted under-performing and characterized by significant scattering of results; this further demonstrates that, due to the poor production control, the batch was already characterized by a strong heterogeneity prior to the samples preparation. It is fair to note, however, that in Reference SB specimens the orientation of fibers was additionally enhanced by controlling the casting flow with a small slide, while, in Used SB, the fresh-state composite was just vertically dropped in the mold, simulating the real production procedures. Two equivalent residual values, f_{eq1} for the Serviceability Limit State (SLS) and f_{eq2} for the Ultimate Limit State (ULS), were averaged on two assigned COD ranges, namely $3{\cdot}w_I \le \text{COD} \le 5{\cdot}w_I$ and $0.8{\cdot}w_u \le \text{COD} \le 1.2{\cdot}w_u$, where w_I is the first cracking COD, identified at the maximum nominal stress value in the interval $0 \le \text{COD} \le 0.1$ mm, and w_u is equal to 3 mm.

Considering a multilinear post-cracking behavior, as suggested by the MC2010, two responses based on strengths f_{Fts} and f_{Ftu}, respectively associated to crack openings w of 0.5 mm (SLS) and 2.5 mm (ULS), were obtained (Fig. 4(d)). In case of notched beam specimens (non-oriented fiber rienforced concrete) $f_{Fts}^{RB} = 0.45{\cdot}f_{R1} = 3.75$ MPa and $f_{Ftu}^{RB} = 0.5{\cdot}f_{R3} - 0.2{\cdot}f_{R1} = 1.84$ MPa, while in case of *structural* specimens (recalled in the following as “oriented material” because of the partial orientation favored by the small thickness and the wall effect), adopting a similar approach, $f_{Fts}^{SB} = 0.45{\cdot}f_{eq1} = 5.40$ MPa and $f_{Ftu}^{SB} = 0.5{\cdot}f_{eq2} - 0.2{\cdot}f_{eq1} = 4.36$ MPa. Two orientation factors K_1 and K_2 were estimated on the average reference values as the ratios $K_1 = f_{Fts}^{RB}/f_{Fts}^{SB} = 0.69$ and $K_2 = f_{Ftu}^{RB}/f_{Ftu}^{SB} = 0.42$, and the average constitutive law of Fig. 4(d) was finally built, combining the identified post-cracking responses with the MC2010 plain concrete stress-strain and stress-crack opening relations for uniaxial tension. To this aim, a C120 concrete grade was considered, as confirmed by 27 compressive tests carried out on 100 mm size cube specimens according to the UNI EN 12390-3 Standard [26] ($f_{cc,av}$ = 138.8 MPa).

2.2. TRC

Textile Reinforced Concrete is a composite material obtained by embedding varied kinds of high tensile capacity fabrics within a fine-grained concrete. Among different reinforcement technologies investigated in the preliminary optimization phase, that included glass, carbon, aramid and basalt fibers, an Alkali-Resistant (AR) glass fabric (Table 4), impregnated with a styrene-butadiene rubber (SBR), was selected for its limited cost and its controlled loss of strength when exposed to a cementitious environment [27]; as confirmed by recent results [28], the strength loss of AR-glass in an alkaline environment is

Table 3
Residual tensile properties of the considered HPFRCCs.

HPFRCC material	Reference				Used			
Specimens (n.)	RB (3)		SB (5)		RB (10)		SB (5)	
Residual strength	f_{R1}	f_{R3}	f_{eq1}	f_{eq2}	f_{R1}	f_{R3}	f_{eq1}	f_{eq2}
Average value $f_{Ri,m}$, $f_{eqi,m}$ [MPa]	15.46	12.87	15.33	24.45	8.33	7.00	12.00	13.53
Coefficient of variation [%]	2.6	11.2	5.1	5.0	43.5	49.3	38.6	61.0
Characteristic value (lognormal) $f_{Ri,k}$ [MPa]	14.17	8.87	13.61	21.67	3.30	2.74	4.21	1.53

Table 4
Fabric specifications.

Characteristic	
Material	AR-glass
Fabrication technique	Leno weave
Warp wire spacing [mm]	~5
Weft wire spacing [mm]	~12.5
Warp fineness [tex]	2 × 1200
Weft fineness [tex]	2400
Warp cross-sectional area [mm^2/m]	179.10
Weft cross-sectional area [mm^2/m]	62.69
Warp avg. tensile load on 70 mm [kN]	10.99
Weft avg. tensile load on 70 mm [kN]	6.23

Table 5
Mix design of the used HPC (w/c = 0.37, w/b = 0.20).

Component	Dosage
Cement I 52.5	609 kg/m^3
Sand 0–2 mm	860 kg/m^3
Water	228 l/m^3
Superplasticizer	28 kg/m^3
Blast furnace slag	507 kg/m^3

generally limited to about 20%. Regarding the matrix, the High Performance Concrete (HPC) admixture of Table 5 was defined by simply removing steel microfibers from the HPFRCC mix of Table 2, readjusting the specific dosages.

As introduced in Fig. 1, the 10 mm thick TRC layer forms the bottom face of the sandwich panel. The orthotropic composite behavior was explored by testing 10 ×70 ×400 mm^3 (free length ℓ_0 equal to ~300 mm) specimens in uniaxial tension, wherein three specimens were prepared for both warp and weft reinforcing directions. The samples ends were clamped by means of a pneumatic system and a constant stroke rate of 0.02 mm/s was assumed as the feedback parameter of a 30 kN electromechanical press.

The results, referring to composites reinforced with a single layer of AR-glass fabric placed in a barycentric position, are displayed in Fig. 5, in terms of average responses, solid-hatched dispersion of results, comparison with the average plain fabric responses (uniaxial tensile tests on 70 ×400 mm^2 strips, free length equal to ~300 mm) and cracking patterns at failure.

A transverse clamping force of about 12 kN was imposed over an area of 70 × 50 mm^2, through 3 mm thick steel plates glued on the specimens to avoid stress concentrations. Despite this, the failure modes were affected by fabric end slippage phenomena, as proved by the pronounced loss of stiffness detectable on the post-cracking branches. It is believed that the inability to fully exploit the AR-glass bearing capacity was mostly related to the inadequacy of the clamping surfaces; as a matter of fact, recent recommendations for TRC uniaxial tensile tests [29,30] suggest a load introduction zone twice as much to the one considered in this campaign. Turning to the real application – characterized by uneven tensile stress distributions, with maximum values located far from the TRC edges – the experimental results were nevertheless considered sufficient to derive the simplified constitutive law implemented in the plane-section analyses.

3. Prototypes preparation

In the sequence of the material choices and mechanical characterization, ten nominally identical full-scale prototypes were produced in a prefabrication plant. Operational procedures were slightly adjusted along the way, to address minor issues such as the buoyancy of the insulating core and the control of the cement-based composites thickness.

The manufacturing steps can be summarized as follows: (i) five 0.2 × 1 × 2.5 m^3 EPS 100 boards were preliminary shaped according to the transverse section of Fig. 1 and glued together to form a monolithic core; (ii) four strips of AR-glass fabrics were cut from a 1.48 m wide roll and spot-glued on the bottom face of the polystyrene (Fig. 6(a)), ensuring an overlap length of about 0.3 m and a double-sided bond with the cementitious matrix. Since the fabric was characterized by a highly orthotropic behavior, the stronger warp was aligned to the transverse panel direction, devoid of ordinary steel reinforcement; (iii) additional fabrics were glued on the top core surfaces, with the aim of providing extra robustness and stabilizing the HPFRCC cracking mechanism; (iv) following the casting of the HPC intrados (Fig. 6(b)), the fabric-reinforced core was put in place, together with the longitudinal steel bars and the anchoring systems; (v) once the middle HPFRCC layer was cast on the top EPS face, reaching through the perimeter the bottom fresh-state HPC, a second steel formwork was positioned (Fig. 6(c)); (vi) the panel was completed with the last HPFRCC batch and demolded after a night of steam curing. As shown in (Fig. 6(d)), the uplifting of the polystyrene due to the hydrostatic pressure was hampered by the insertion of a series of distribution plates connected to contrast rods. This obviously represents a first attempt solution, that should be improved in the future whether an effective water-tightness of the exposed surface needs to be achieved.

4. Full-scale bending tests

The main objective of the present paper is the discussion of real scale bending tests on roof elements prototypes. In particular, two elements were tested according to a longitudinal bending scheme, while a transverse bending loading scheme was used to test other two structural elements. All the tests were performed with an electromechanical jack with a maximum loading capacity of 1000 kN.

Regarding the longitudinal bending (LB) tests, a four-point bending scheme was adopted: the roof elements were simply supported over two linear steel supports, characterized by a width of 160 mm and placed exactly at the end of the elements. A 5 mm thick neoprene sheet was placed between the bottom surface of the prototype and each linear support to avoid stress localization due to the not perfect contact between the two surfaces. These supports are schematized in Fig. 7(a) as a linear support at 80 mm from the edge. Two steel loading knives, 3 m long, were directly connected to the jack head and were used to apply the load over the top surface of the two external ribs, again through a 5 mm thick neoprene sheet. The adopted shear span (a_{LB}) was equal to 1670 mm, while the constant bending moment region was 1500 mm wide. All the tests were displacement controlled using the jack head displacement (stroke) as feedback parameter; a displacement rate ranging between 15 µm/s and 45 µm/s was imposed. In order to better

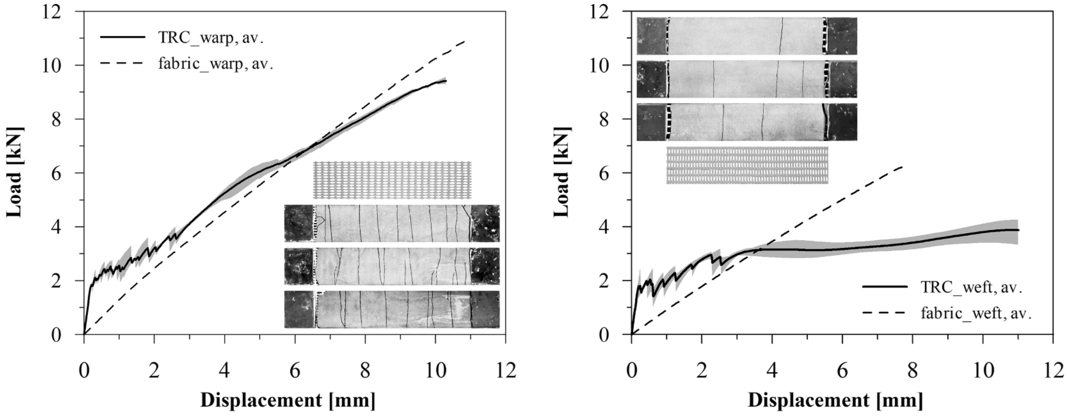

(a)

(b)

Fig. 5. TRC mechanical response in uniaxial tension along the warp (a) and weft (b) fabric directions.

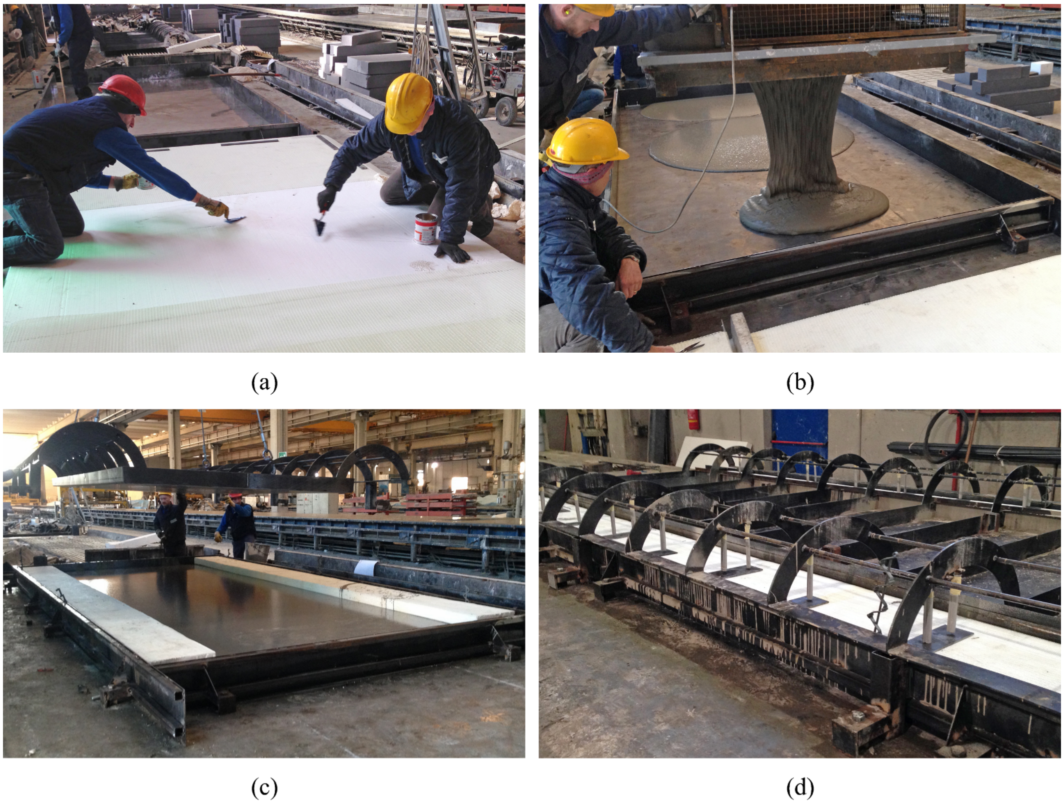

(a)

(b)

(c)

(d)

Fig. 6. Prototypes production phases: AR-glass fabrics gluing (a), casting of the HPC intrados (b), positioning of the second steel formwork (c) and system introduced to contrast the EPS uplifting (d).

comprehend the structural behavior of the element, a proper set of instruments was installed to monitor the specimen response. In particular, three Potentiometer Displacement Transducers (PDT) with maximum stroke equal to 150 mm were used to measure the mid-span deflection at the center of the specimen width (δ1) and close to the lateral edge, respectively at the center of the lateral ribs (δ2 and δ3). Two additional PDTs (δ4 and δ5), with stroke equal to 50 mm, were used to measure the deflections close to the supports, just 310 mm far away from the roof element shorter sides. Three PDTs (COD1,2,3) were applied to the specimen bottom surface to measure crack opening displacement astride the constant bending moment region, with a gage length equal to 1600 mm. As many transducers of the same type (COM1,2,3) were glued on the specimen upper surface to record axial compression displacement over a gage length equal to 1 m. The position of all the displacement transducers, as well as the loading schemes and the specimen geometry are given in Fig. 7(a). All the instruments signals were recorded by a Data Acquisition System with a measuring rate equal to 1 Hz and with a 16-bit precision.

Regarding the transverse bending (TB) tests, the same loading knives and the same steel linear supports previously described for longitudinal bending, were adopted. The loading scheme and the instrumentation are represented in Fig. 7(b), where it is possible to point out that supports and loading lines, both 3 m long, did not cover the whole length of the specimen and were hence placed at its center. A four-point bending test setup was adopted also in this case, considering a shear span (a_{TB}) equal to 870 mm and a distance between the loading points equal to 600 mm. Three P DTs (stroke 150 mm) were used to measure mid-span deflection: in particular, one (δ1) was placed exactly

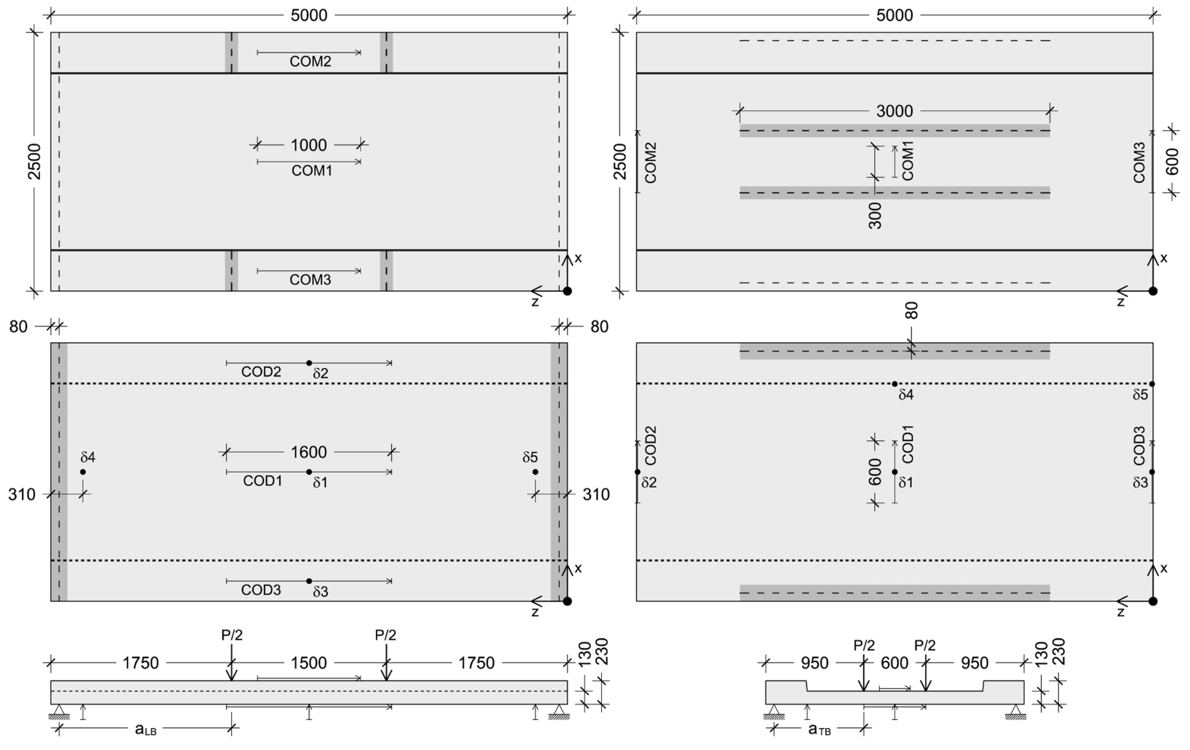

(a) (b)

Fig. 7. Top, bottom and side views of the instrumented prototypes tested in longitudinal (a) and transverse (b) bending. Please note that the darker solid hatches represent the neoprene sheets introduced to prevent stress concentration (measures expressed in mm).

at the center of the roof element, while the remaining two ($\delta 2$ and $\delta 3$) were located close to the specimen edges. The deflections at the positions characterized by the change of the cross-section depth (both at the center and close to the edge) were measured by two additional PDTs ($\delta 4$ and $\delta 5$, stroke 50 mm), just on one side. Crack opening displacement at the center of the specimen (COD1) was measured by a 10 mm stroke displacement transducer, placed on the bottom surface of the element over a gage length equal to 600 mm. Two additional displacement transducers (COD2,3) were used to measure crack opening propagation close to the edge of the bottom surface. In the same location, but on the upper face of the specimen, three transducers (COM1,2,3) were applied to measure the compressive strain over gage lengths respectively equal to 300, 600 and 600 mm. It is worth to note that all the instruments close to the border of the specimen (COD2,3 and COM2,3) were instrumental also to take into account the load diffusion, due to the fact that, as mentioned, both the loading knives and the supports did not cover the whole length of the specimen.

4.1. Longitudinal bending results

The experimental behavior of the two nominally identical panels tested according to a longitudinal bending (LB) setup is presented in Fig. 8, in terms of Load (P) vs. Stroke/Displacement (Stroke/$\delta 1$), Moment (M) vs. Curvature (ϑ) and Moment vs. COD/COM diagrams; bending moment was evaluated as $M = P/2{\cdot}a_{LB}$, while the i-th curvature was estimated as follows:

$$\vartheta i = \frac{CODi/GL_{COD,i} + COMi/GL_{COM,i}}{h_i} \qquad (1)$$

with COD_i and COM_i taken with the signs of Fig. 8 (please refer to the caption) and where $GL_{COD,i}$, $GL_{COM,i}$ and h_i respectively represent the gage length of the i-th intrados transducer, the gage length of the i-th extrados transducer and the distance amid the outermost chords of the considered section, i.e. 130 or 230 mm.

In Fig. 8(a) it is possible to observe the comparison between the stroke displacement, as recorded at the jack head, and the displacement measured by the potentiometer $\delta 1$. Please note that the small plateaus exhibited by the stroke measures at about 9 and 19 kN were associated to the testing frame mechanical interplays. It is also important to mention that, before the peak load was reached, safety concerns always led to the samples unloading and the early removal of the transducers; in this sense, only the load-stroke diagrams must be considered representative of the panel responses up to the end of the tests.

Even though the mechanical behavior of the two LB samples appeared to be similar up to a load of about 80 kN, the collapse was associated to different mechanisms. As displayed in Fig. 9(a), specimen LB1 failed due to the widening of a flexural crack located between the loading knives; on the contrary, as shown in Fig. 9(b), specimen LB2 suffered a premature softening, triggered by the unsymmetrical shear cracking of a lateral web. Unfortunately, LB1_COM1 data went missing at $M \approx 31$ kNm ($P \approx 37$ kN) due to a communication problem, but since the transducers were de-installed before the onset of the ultimate modes, the LB2_COM1 trend may be considered sufficiently re-presentative of both the panels (Fig. 8(d)).

Fig. 8(b) shows that, while specimen LB1 was characterized by rather uniform M-ϑi responses, prototype LB2 experienced a delayed deformation of its central region, as entailed by an unbalanced flexural stiffness; as a matter of fact, the intrados area monitored by the LB2_COD1 transducer (Fig. 8(c)) started cracking only at $M \approx 26$ kNm ($P \approx 31$ kN). It is also interesting to observe that the middle HPFRCC plate, initially subjected to a weak compression, switched to a tensile state of stress at $M \approx 32$ kNm ($P \approx 38$ kN), with a pronounced slope variation at $M \approx 42$ kNm ($P \approx 50$ kN). The sharp change of the LB2_COM1 output could be related to a drop of stiffness at the bottom layer, as exhibited by a cracked TRC: considering the average $\mathrm{COD_{av}}$ at $M = 42$ kNm, an equivalent tensile strain can be calculated as $\mathrm{COD_{av}}/\mathrm{GL_{COD}} = 1.75\ \mathrm{mm}/1600\ \mathrm{mm} = 0.11\%$; referring to Fig. 5(b) and roughly considering a normalized displacement (δ/ℓ_0) of the same order

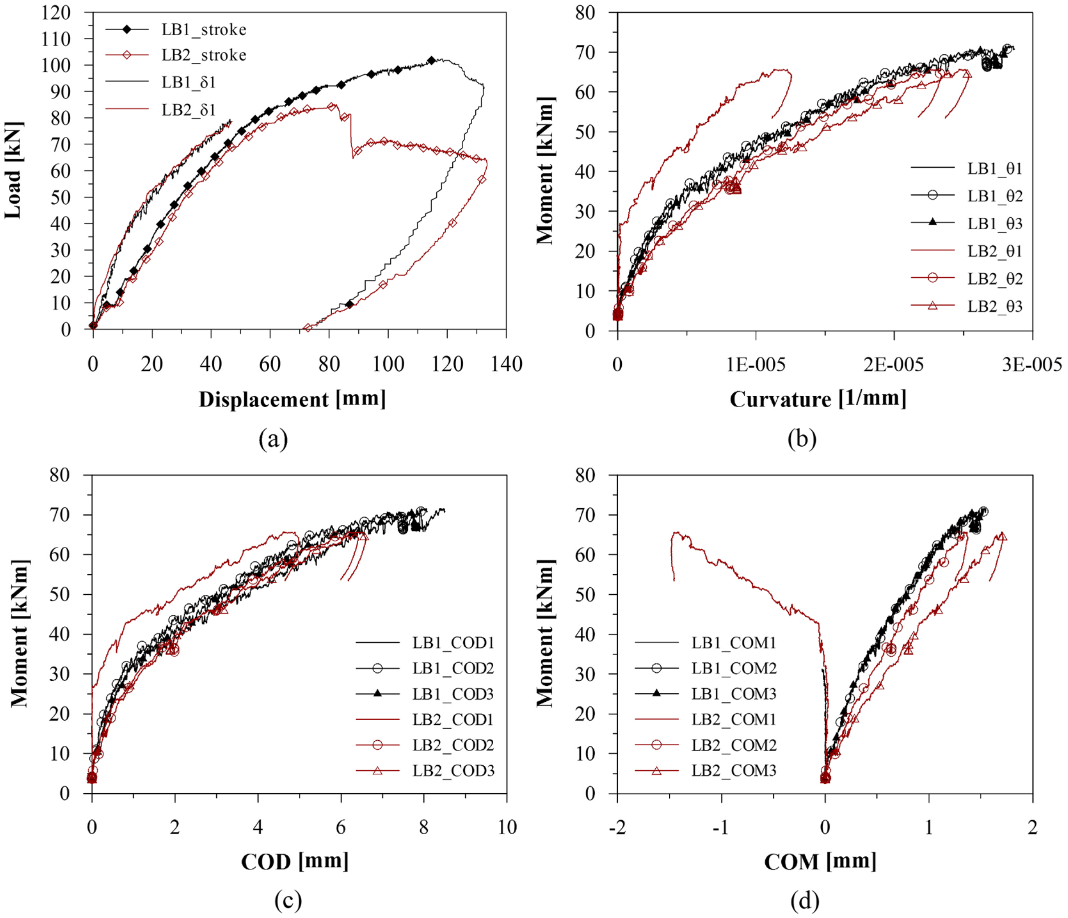

(a) (b)

(c) (d)

Fig. 8. Full-scale longitudinal bending (LB1, LB2) tests: Load vs. Displacement (a), Moment vs. Curvature (b), Moment vs. Crack Opening Displacement (c) and Moment vs. Compressive Displacement (d) experimental results. Please note that positive outputs respectively represent a COD elongation and a COM contraction.

of magnitude, it is possible to notice that the value corresponds to the beginning of the TRC multi-cracking phase.

The considerable shifting of the neutral axis is confirmed also by the LB1 crack pattern analysis of Fig. 9(c), in which it appears that, focusing on the middle plate, additional flexural cracks were activated and the pre-existing ones were quickly widened at a load P greater than 45 kN. To better understand the prototypes responses, HPFRCC cores were drilled and measured at relevant positions (numbers and letters in Fig. 9(c)). According to the data collected in Table 6, it is possible to conclude that panel LB2 was penalized by thinner extrados layers, most likely to be due to the uncontrolled buoyancy of the EPS core. The reduced thickness further explains the different mechanical response highlighted in Fig. 8, the unsymmetrical diffusion of the applied load from the external ribs towards the center and the mentioned unexpected propagation of shear cracks. To this aim, it should be noted that the region displayed in Fig. 9(b) was close to coring A, characterized by a top plate thickness of only 9 mm and a web thickness of only 12 mm (both to be compared with the 20 mm nominal thicknesses of Fig. 1).

4.2. *Transverse bending results*

In Fig. 10, the results pertaining to the two nominally identical panels tested according to a transverse bending (TB) scheme are presented in terms of Load (P) vs. Stroke/Displacement (Stroke/δ1), Bending moment (M) vs. Curvature (ϑ) and Bending moment vs. COD/COM diagrams. The bending moment was evaluated as $M = P/2{\cdot}(a_{TB})$, while the curvature was calculated according to Eq. (1), considering $h_i = 130$ mm. Also in this situation, the two prototypes exhibited different failure mechanisms: the peak load of test TB1 was associated to the localization of a flexural crack initially developed at the midspan of the HPFRCC end plate (Fig. 11(a)), while specimen TB2 experienced an early failure caused by the delamination of the TRC bottom layer (Fig. 11(b)). As depicted in Fig. 11(c), prototype TB1 underwent the development of circular plastic hinges on the middle HPFRCC layer, which behave as a quasi-brittle thin plate supported by a soft elastic material.

The continuity of the middle HPFRCC plate was firstly lost in the x direction (see the cracks at $P = 65$ kN and $P = 100$ kN in Fig. 11(c)), leading to a greater out-of-plane loading of the TRC intrados; the loss of stiffness of this central area, worsened by the release also in the z direction, finally favored the development of a dense cracking pattern in the TRC outer regions (stiffened by the 20 mm thick HPFRCC head plates). This mechanism is confirmed by the measures displayed in Fig. 10, where it is possible to observe the limited vertical displacement at the bottom level (TB1_δ1), the delayed cracking of the TRC (TB1_COD1) and the complete absence of compressive strains in the central region (TB1_COM1 in Fig. 10(d)). Even though localization occurred within the area monitored by the transducer TB1_COD2 (i.e. close to coring D of Fig. 11(c)), for a fixed value of M, curvature $\vartheta 3$ appears to be larger than $\vartheta 2$; this can be explained by the fact that, according to the reconstructed pattern, much more cracks were developed across the TB1_COD3 gage length, but none of them led to a localization.

Regarding prototype TB2, delamination was explained by the fact that, in order to prevent the core uplifting, the HPFRCC was cast on a slightly hardened HPC (60 min of curing were imposed between the two batches). In the absence of dedicated shear connectors, the weakened

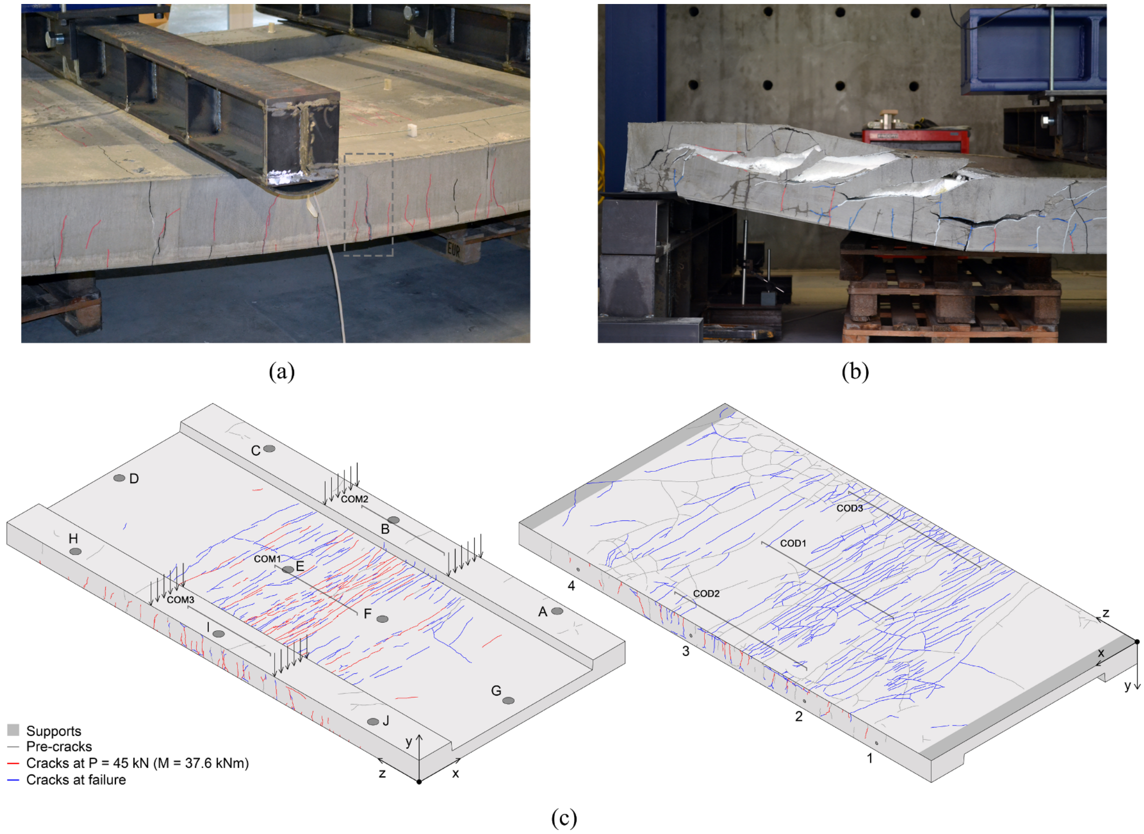
(a)

(b)

(c)

Fig. 9. Longitudinal bending tests: failure modes of prototypes LB1 (a) and LB2 (b) and crack patterns of prototype LB1 (c); please note that since the intrados cracks could be safely traced only at the end of the tests, it was not possible to distinguish the opening of cracks among different loading levels. Numbers and letters indicate the coring positions (Φ20 and Φ100 mm in diameter, respectively).

Table 6
HPFRCC thickness [mm] at different coring locations (please refer to Figs. 9(c) and 11(c)).

	A	B	C	D	E	F	G	H	I	J	1	2	3	4
LB1	20	26	18	17	17	17	21	31	27	30	22	20	20	18
LB2	9	23	14	8	20	18	10	10	27	12	12	20	19	21
TB1	20	26	20	20	16	20	19	22	27	25	23	29	15	19
TB2	20	21	11	22	11	17	17	25	22	13	19	20	19	21

interface hindered the activation of the mentioned plastic hinges and the subsequent vertical crushing of the EPS.

In Fig. 10(a) it is possible to notice that, net of the frame interplays, the output TB2_δ1 does not substantially differ from the jack head displacement and in Fig. 10(d), where the strong difference between the TB2_COM1 and the TB1_COM1 outputs can be appreciated. Strain localization again occurred on the outer zones, with some lag on the side hosting the transducers TB2_COM3 and TB2_COD3, opposite to the head of Fig. 11(b).

5. Plane-section analyses

To assess the reliability of simplified design models as an easy engineering approach, plane-section (PS) analyses were carried out by imposing an increasing curvature over the section, calculating the corresponding bending moments through the integration of stresses; known the M-ϑ sectional responses, the P-δ structural behaviors were finally obtained by equilibrium and integration of curvatures. The analytical investigations targeted the longitudinal bending tests, on account of the efficacy of the Euler-Bernoulli kinematic model in simulating the responses discussed in Section 4. Shear deformability was not deemed relevant since the softness of the EPS core was controlled by the presence of the two HPFRCC ribs working in parallel (a box-like panel behavior was observed). Nevertheless, it should be noted that the EPS plays a role in ensuring the applicability of the plane-section approach, because its ability to work in compression along the y axis limits the transverse deformability of the section (especially in the central region, where the effect of the ribs is less relevant).

Cement-based composites and steel bars were respectively accounted for by means of average multilinear and bilinear laws retrieved from the characterization campaign (Section 2), while the EPS was omitted due to its negligible contribution resulting from its very low elastic modulus. Concerning the HPFRCC, mode I stress-strain relations were derived from the stress-crack opening results (Fig. 4(d)), by smearing w over a characteristic length ℓ_{cs}, such that $\varepsilon = w/\ell_{cs}$ [31]. As shown in recent works, better predictions of the mechanical response of fiber-reinforced structural elements can be obtained by considering multiple characteristic lengths within the cross-section [32], as displayed in Fig. 12(a) (ℓ_{csA}-ℓ_{csD}). Since the employed algorithm was based on material properties that could vary only along the section depth, two values $\ell_{cs1} = \ell_{csA}$ and $\ell_{cs2} = \ell_{csD}$ were introduced; the first, ℓ_{cs1}, was assigned to the area hosting the longitudinal steel bars (first 100 mm measured from the HPFRCC bottom chord), while the second, ℓ_{cs2}, was attributed to the extrados region (from the middle plate upwards, as displayed in Fig. 12(b)); considering the small contribution of the webs in the ℓ_{cs2} region on the overall behavior, such simplification was considered acceptable.

According to the MC2010, the characteristic length ℓ_{cs} of conventionally reinforced FRC elements should be taken as the lowest of:(i) the distance y between the neutral axis and the extreme bottom stretched fiber and (ii) the average spacing s_{rm} between cracks. The

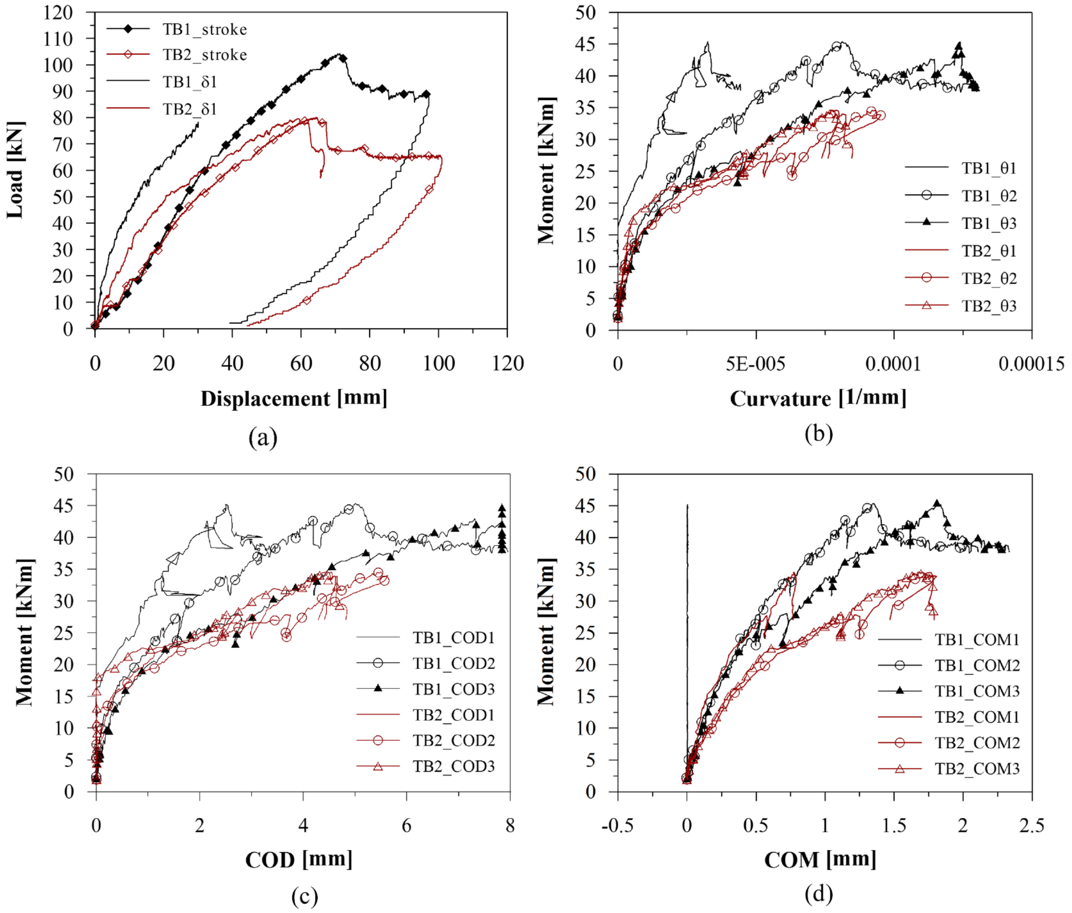

Fig. 10. Full-scale transverse bending (TB1, TB2) tests: Load vs. Displacement (a), Specific moment vs. Curvature (b), Specific moment vs. Crack Opening Displacement (c) and Specific moment vs. Compressive Displacement (d) experimental results. Please note that positive outputs respectively represent a COD elongation and a COM contraction.

former value is measured from a neutral axis *n-n* estimated in a cracked situation, in which both the tensile strength of concrete and the contribution of fibers are neglected (Fig. 13(b)).

Given these hypotheses and considering only the HP FRCC depth *h*, since the characteristic length should be intended as a local material property, *y* takes the value of 193.1 mm, as shown in Fig. 13(b). The average crack spacing s_{rm} is instead calculated as:

$$s_{rm} = 1.5\left(k\cdot c + \frac{1}{4}\cdot\frac{\phi_s}{\rho_{s,ef}}\cdot\frac{f_{ctm} - f_{Ftsm}}{\tau_{bm}}\right) \tag{2}$$

where *k* is an empirical parameter assumed equal to 1, *c* (28 mm) is the minimum concrete cover, Φ_s (14 mm) is the longitudinal bar diameter, $\rho_{s,ef}$ (1.77%) is the effective reinforcement ratio, calculated as the ratio between the area A_s of the steel bar and the effective area $A_{c,ef}$ (8723.9 mm^2, see Fig. 13(b)) of the HPFRCC in tension, f_{ctm} (5.64 MPa) is the mean tensile strength of the plain C120 concrete, f_{Ftsm} is the average SLS strength calculated in Section 2.1 ($f_{Fts}{}^{RB} = 3.75$ MPa) and τ_{bm} is the mean bond strength between steel and concrete, calculated as $1.8{\cdot}f_{ctm} = 1.8{\cdot}5.64$ MPa = 10.2 MPa.

Being $s_{rm} = 97.4$ mm $< y$, the average crack spacing was identified as the characteristic length ℓ_{cs1} of the HP FRCC surrounding the longitudinal reinforcement. Regarding the extrados area, on account of the lack of traditional reinforcement and the deflection-hardening behavior observed on the *structural* beams (Fig. 4(c)), the characteristic length ℓ_{cs2} was assumed to be equal to the HPFRCC plates nominal thickness, i.e. 20 mm [11]. It is worth noting that, as displayed in Fig. 13(a), the estimated lengths of the fracture process zone are consistent with the crack patterns observed on sample LB1. The resulting constitutive laws are shown in Fig. 14(a), where it is possible to notice that favorable fiber orientation effects were also considered, increasing the post-cracking behavior in line with that already discussed in Section 2.1.

Textile reinforced concrete was modelled by means of a trilinear strain-hardening law (Fig. 14(b)), whose points were identified on the average experimental curve of Fig. 5(b) according to the following procedure: point A was identified by imposing the same elastic modulus assigned to the HP FRCC (46877 MPa, evaluated according to the ISO 1920-10 Standard) to the average first-cracking nominal stress in the weft direction; point B was selected on the same curve, as the point representing the end of the multi-cracking branch (strain was estimated as the ratio between the displacement in the uniaxial tensile test and the free specimen length ℓ_O); point C was found tracing through point B a line parallel to the fabric weft response, limited at its maximum mechanical capacity (6.23 kN of Table 4, divided by the average TRC cross-sectional area). In this sense, considering the large anchoring lengths available on the real structure, a TRC efficiency factor ($P_{peak,TRC}/P_{peak,FABRIC}$) [16] equal to 1 was assumed, overcoming the fabric end slippage observed in Section 2.2.

A series of plane-section analyses was performed (Table 7) and compared with the full-scale tests results (Fig. 15), to confirm the interpretation of the experimental evidences and highlight the contribution of individual materials to the overall mechanical response. In the first two simulations the intrados was omitted and the HP FRCC area, reinforced with the two Φ14 steel bars, was alternately treated as a plain concrete with zero tensile strength (ps1) and a fiber-reinforced composite with two characteristic lengths and the residual tensile

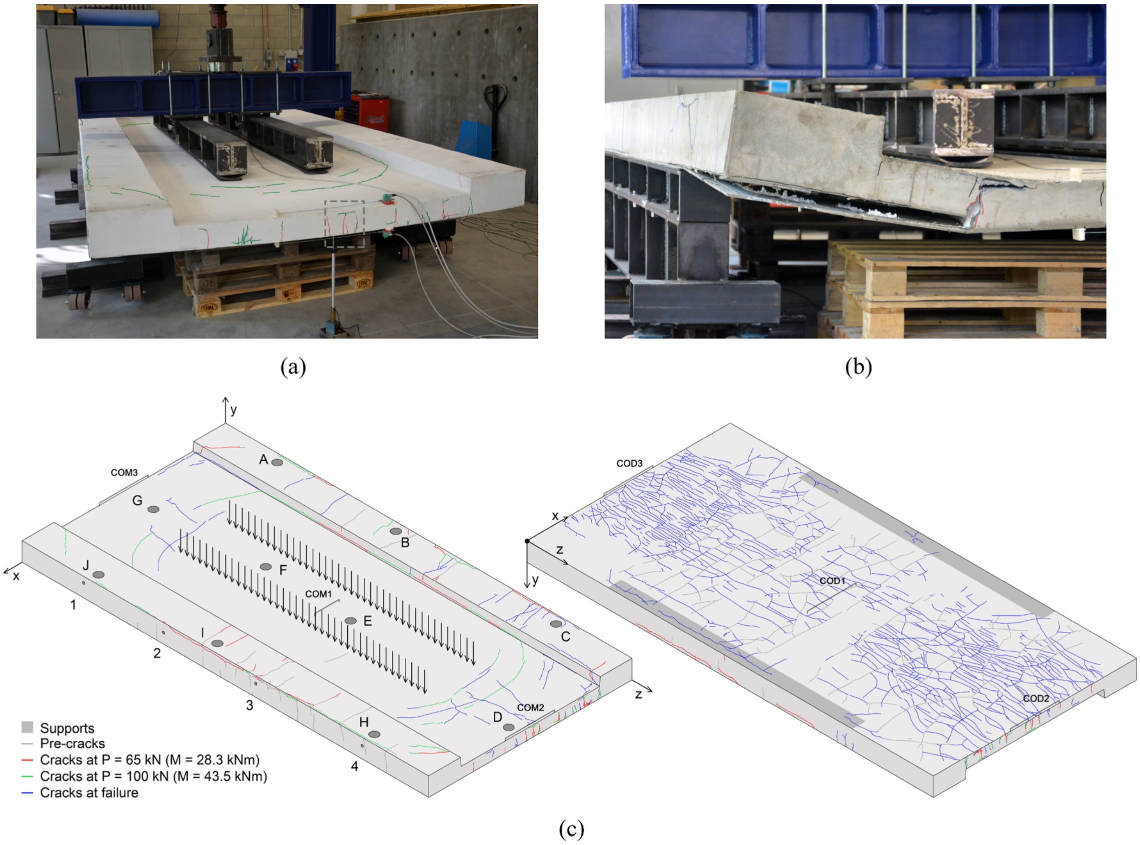
(a)
(b)
(c)

Fig. 11. Transverse bending tests: failure modes of prototypes TB1 (a) and TB2 (b) and crack patterns of prototype TB1 (c); please note that since the intrados cracks could be safely traced only at the end of the tests, it was not possible to distinguish the opening of cracks among different loading levels. Numbers and letters indicate the coring positions (Φ20 and Φ100 mm in diameter, respectively).

behavior of the non-oriented material (ps2). Please note that, referring to the compressive behaviors of the cement-based materials, the C120 grade non-linear law suggested by the MC2010 was implemented in all the algorithms. In simulation ps3, the intrados layer was introduced, assigning the 0-C′ law of Fig. 14(b), representing the plain fabric tensile behavior; the choice of penalizing the TRC – both in terms of initial stiffness and global toughness – was made because the prototypes were affected by the presence of pre-existing cracks (see Fig. 9(c)) resulting from constrained shrinkage and inadequate handling/storage procedures. In simulation ps5 the intrados was described by the complete 0-A-B-C trilinear law and finally, in simulations ps4 and ps6, the effect of fibers orientation was introduced in the ℓ_{cs2} regions. The results are presented in the following, in terms of sectional (M-ϑ) and structural (P-δ) behaviors.

In Fig. 15(a), the analytical M-ϑ curves are compared with the average ones detected on the two prototypes (mean of M-ϑ *2* and M-ϑ *3*); as one should note also in Fig. 15(b), analyses ps3 and ps4 can be considered as reliable predictions of the P-δ experimental responses, in particular with regard to prototype LB1 (characterized by a symmetrical flexural failure and good geometrical tolerances). Since the cracking patterns of Fig. 9(c) proved that the TRC was not fully cracked prior to the tests, it is believed that the most representative behavior may fall between curves ps3 and ps6.

Reference points of Fig. 16 and Table 8 were selected on the ps4 curve, taken as a reference, in order to identify the sequence of typical mechanisms. The first branch (0-A) is characterized by linear-elastic material behaviors (see the stress distributions of Fig. 17), with the exception of the TRC, in which the pre-cracked condition was imposed a priori. The HPFRCC starts cracking on the tensile side of the lateral webs (before point B) and the propagation through the middle plate (phase B-C) occurs at M values comparable with the experimental evidences (see Fig. 9(c)). The development of flexural cracks is followed by the yielding of the steel bars (point C) and by the rupture of the intrados layer (point D).

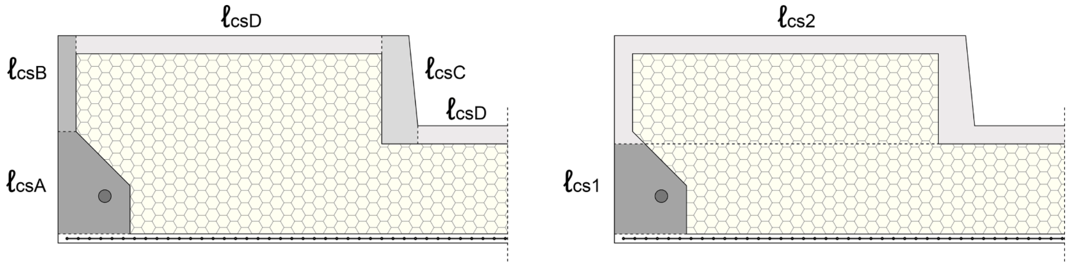
(a)
(b)

Fig. 12. Identification of the material characteristic lengths (a) and simplification considered in the plane-section analyses (b).

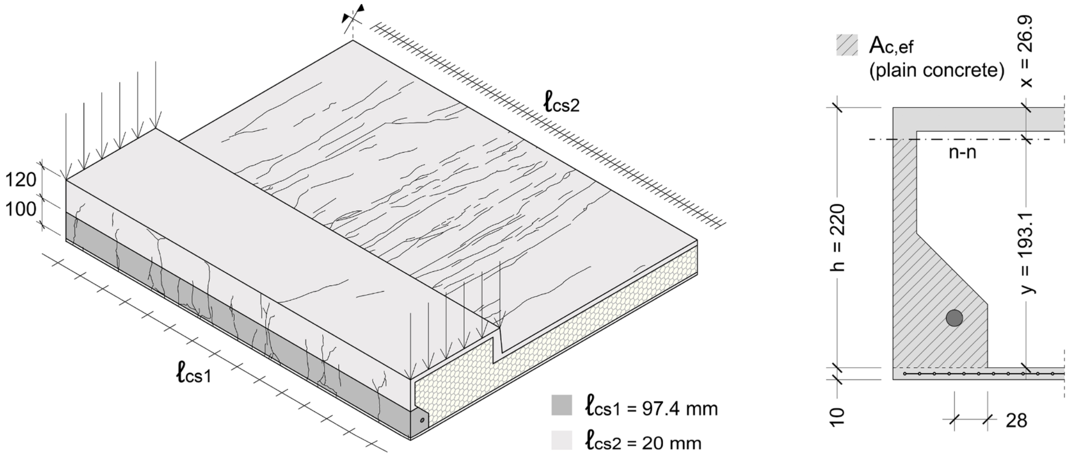

(a) (b)

Fig. 13. Comparison between the calculated and the experimental characteristic lengths, over the constant bending moment region of prototype LB1 (a) and evaluation of the effective HPFRCC area in tension, based on the position of the neutral axis in a plain concrete section, reinforced with the steel bars and the glass fabric (b).

For the sake of completeness, in Fig. 16 the analytical curve is also compared to the peak experimental responses and to the acting design bending moments at serviceability and ultimate limit states (M_{SLS} = 21.9 kNm, M_{ULS} = 30.3 kNm), evaluated assuming a uniformly distributed load consisting of a self-weight of 1.2 kN/m^2, a non-structural dead load of 0.4 kN/m^2 (PV system) and an accidental snow load of 1.2 kN/m^2.

Regarding the transverse direction, the plane-section approach was considered unfit to simulate the entire sectional and structural responses, because of the uneven distribution of loads/supports and the presence of out-of-plane mechanisms, as discussed in Section 4. Considering an ultimate capacity mainly governed by the TRC warp strength, the analysis was confined to the estimation of the peak bending moment *M*. Two alternative results, respectively associated to the whole cross-section and the only external portions (1 + 1 m wide, stiffened by the 20 mm thick head plates) of Fig. 18, take values of 121 kNm and 48.7 kNm, roughly confirming that the resisting mechanism was mostly controlled by the outer regions (see Figs. 10(b) and 11(c)).

Even though the full-scale sample population was not sufficiently large to allow a proper statistical determination of design values assisted by testing [33], by using an indirect approach it is possible to evaluate the allowed standard deviation that satisfies the bending requirement (resisting bending moment M_{Rd} equal to the acting bending moment M_{Sd}). In this regard, the coefficients of variation V_x associated to an assumed infinite number of experiments were estimated by considering the Eurocode 0 – Annex D formulation for the assessment of the design capacity X_d:

$$X_d = \frac{\eta_d}{\gamma_m} m_X (1 - k_n \cdot V_x) \tag{3}$$

Reversing Eq. (3) and considering a conversion factor η_d equal to 1, a partial factor γ_m of 1.5 (typical of cement-based materials), average values m_x corresponding to the average experimental peak responses (78.2 kNm for LB and 13.4 kNm/m for TB), a characteristic fractile factor k_n equal to 1.64 and design values X_d coincident with the ULS demands (30.3 kNm for LB and 3.0 kNm/m for TB), the admissible coefficients of variation V_x take values of 25.5% for the longitudinal bending and 40.2% for the transverse bending. Despite the scarcely repeatable responses discussed in Section 4, the experimental coefficients of variation V_x (to a preliminary attempt calculated on the basis of the limited experimental results) are lower than the admissible ones (12.9% < 25.5% for LB and 18.6% < 40.2% for TB) and, conse-quently, it can be assumed that a controlled production could easily satisfy the requirements of a design by testing procedure.

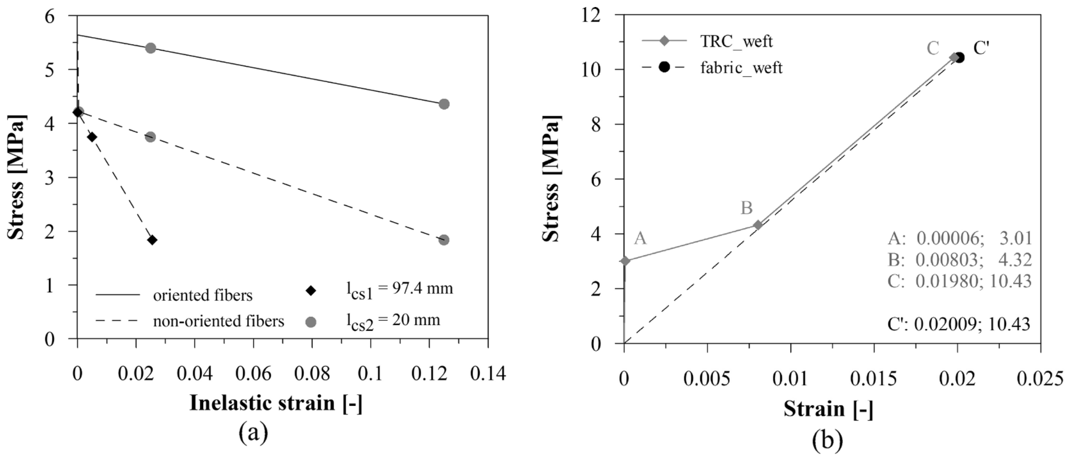

(a) (b)

Fig. 14. HPFRCC mode I stress-inelastic strain laws (a) and TRC tensile laws (b) implemented in the PS analyses. Please note that the last points of the constitutive laws were always followed by a zero tensile strength.

Table 7
Summary of the performed plane-section analyses. Peak curvatures of analyses ps1 and ps2 are omitted, being associated to failure mechanisms different from the ones observed on the full-scale panels.

Analysis	Intrados	Extrados	$\vartheta_{peak,PS}$ [1/mm]	$M_{peak,PS}$ [kNm]	$\frac{M_{peak,PS}}{M_{peak,LB1}}$	$\frac{M_{peak,PS}}{M_{peak,LB2}}$
ps1	–	plain concrete (f_{ct} = 0)	–	29.50	0.35	0.41
ps2	–	non-oriented, ℓ_{cs1} + non-oriented, ℓ_{cs2}	–	53.00	0.62	0.75
ps3	fabric	non-oriented, ℓ_{cs1} + non-oriented, ℓ_{cs2}	9.37e−5	109.00	1.28	1.53
ps4	fabric	non-oriented, ℓ_{cs1} + oriented, ℓ_{cs2}	9.47e−5	115.00	1.35	1.62
ps5	TRC	non-oriented, ℓ_{cs1} + non-oriented, ℓ_{cs2}	9.42e−5	110.00	1.29	1.55
ps6	TRC	non-oriented, ℓ_{cs1} + oriented, ℓ_{cs2}	9.52e−5	116.00	1.36	1.63

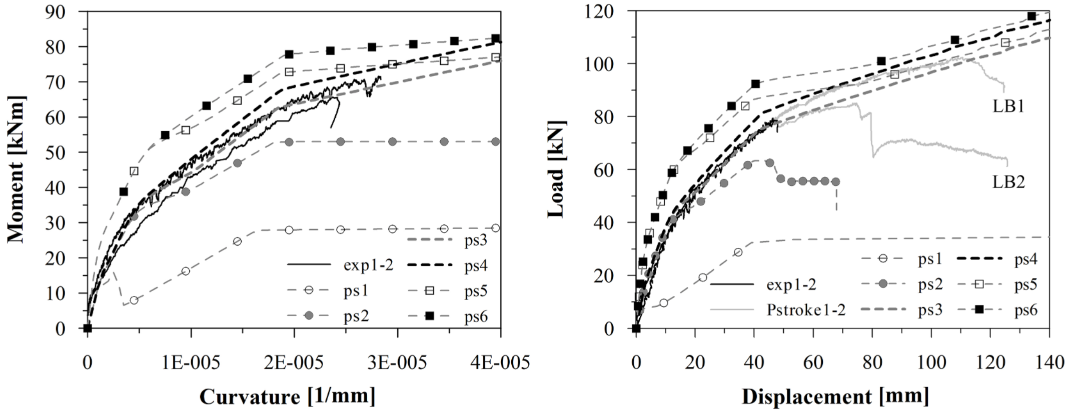

(a) (b)

Fig. 15. Comparison between the analytical and the LB experimental results: bending moment vs. curvature (a) and load vs. displacement (b) diagrams. Please note that the plots are interrupted at a fixed curvature/displacement value, to allow a better inspection of the analytical results.

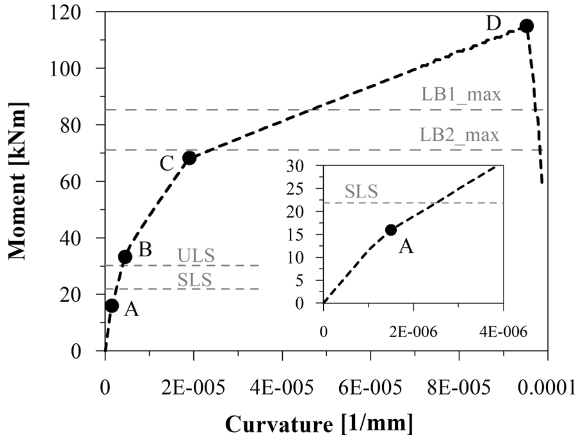

Fig. 16. Reference points on the ps4 moment-curvature diagram and comparison with the experimental (LB1 max, LB2 max) and the acting design bending moments (SLS, ULS).

Table 8
Description of the sectional response in plane-section analysis ps4.

Phase	Description
0-A	Elastic, with pre-cracked intrados
A-B	HPFRCC cracking on the lateral webs
B-C	HPFRCC cracking on the middle plate
C-D	Yielding of the steel bars
Point D	Rupture of the intrados

6. Concluding remarks

Based on the experimental results and the simplified simulations, it is possible to draw the following conclusions.

1. Environmental sustainability can be improved by integrating thermal insulation and energy production within the same structural component. In this field, advanced cement-based materials can play an important role, since the lightness associated to the reduced structural thickness positively impacts production, storage, transportation and dismantling costs. Within the framework of industrial building retrofitting, lighter roof elements imply a significant decrease of inertia-induced forces, automatically improving the structural safety of existing beams, walls, columns and foundations.
2. As confirmed by the characterization tests at the material level, the technological transfer of high-performance composites from the laboratory scale to the precast plant may involve undesirable phenomena like poor control over the fiber distribution. In order to achieve smaller scattering of results, an improvement of the technological preparation procedure is needed, to significantly reduce the measured standard deviations.
3. Materials such as HPFRCC and TRC can be effectively employed in innovative multilayered panels, thanks to their excellent tensile behaviors, respectively provided by high-carbon steel microfibers and AR-glass textiles. The bending behaviors exhibited by the full-scale prototypes were characterized by a significant structural response, in terms of strength, ductility and robustness. The comparison between the average peak bearing capacities and the estimated ULS actions gives loading ratios of ∼2.6 in case of longitudinal bending and ∼4.4 in case of transverse bending.
4. In longitudinal bending, sectional and structural behaviors can be

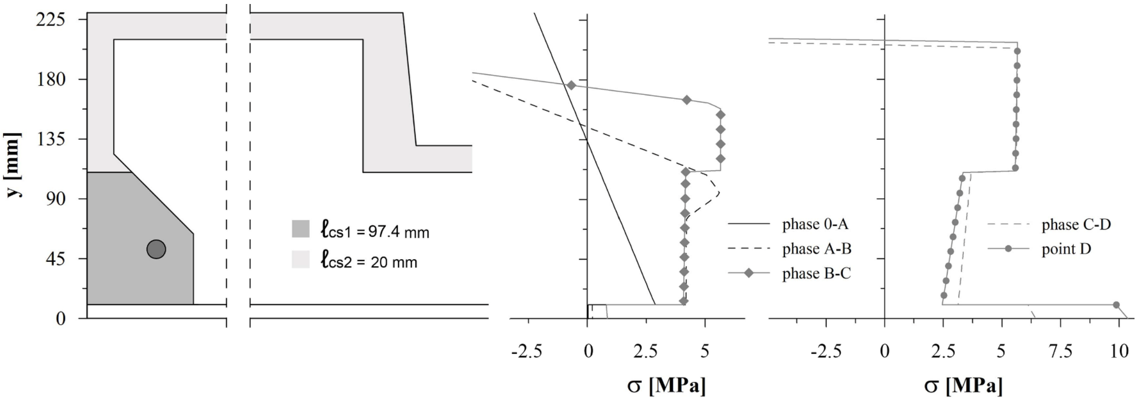

Fig. 17. Analytical stress distributions on the prototypes section, in the reference phases of Table 8.

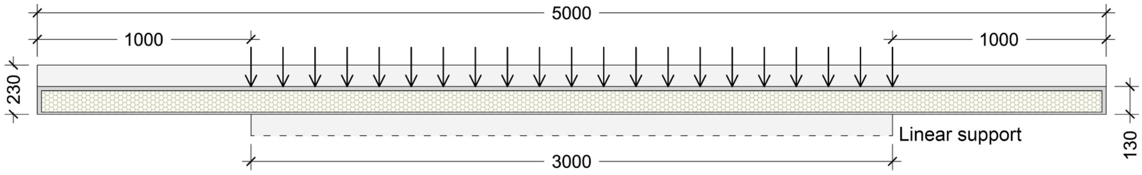

Fig. 18. Transverse section considered in the plane-section analyses (transverse bending case).

successfully simulated by means of simplified plane-section approaches. In spite of the introduction of a strong hypothesis such as the Euler-Bernoulli kinematic model, the results confirm the reliability of the design method, even though the peak loads and ultimate displacements were over-estimated due to the inability to represent all the observed heterogeneities.

5. In transverse bending the resisting mechanism was rather complex, hence difficult to simulate with simplified approaches. Given the non-uniform distribution of load/supports, the global behavior was strongly influenced by the out-of-plane response of the thin cement-based layers.
6. Although the prototypes exhibited considerable structural capacities, unexpected failure modes were activated by the lack of thickness control. Further developments should hence focus on the refinement of the production procedures, also in the interest of preventing pre-existing cracks.

Acknowledgements

The authors would like to acknowledge MEng. Luca Gussoni and Mr. Andrea Stefanoni for their help in the experimental campaign. This work was supported by Regione Lombardia and by the Italian Ministry of Education, Universities and Research [decree number 7128 of July 29th, 2011].

References

[1] CRESME. Il mercato immobiliare in Regione Lombardia nel 2014 (in Italian); 2015.
[2] Vinson JR. Sandwich structures. Appl Mech Rev 2001;54(3):201–14.
[3] di Prisco M, Ferrara L, Lamperti M, Lapolla S, Magri A, Zani G. Sustainable roof elements: a proposal offered by cementitious composites technology. In: Fardis M, editor. Innovative materials and techniques in concrete construction. Dordrecht: Springer; 2012. p. 167–81.
[4] Dey V, Zani G, Colombo M, di Prisco M, Mobasher B. Flexural impact response of textile-reinforced aerated concrete sandwich panels. Mater Des 2015;86:187–97. https://doi.org/10.1016/j.matdes.2015.07.004.
[5] Colombo I, Colombo M, di Prisco M. Bending behaviour of Textile Reinforced Concrete sandwich beams. Constr Build Mater 2015;95:675–85.
[6] Shams A, Stark A, Hoogen F, Hegger J, Schneider H. Innovative sandwich structures made of high performance concrete and foamed polyurethane. Compos Struct 2015;121:271–9.
[7] Shams A, Horstmann M, Hegger J. Experimental investigations on Textile-Reinforced Concrete (TRC) sandwich sections. Compos Struct 2014;118:643–53.
[8] Stark A, Classen M, Knorrek C, Camps B, Hegger J. Sandwich panels with folded plate and doubly curved UHPFRC facings. Struct Concrete 2018;19(6):1851–61.
[9] Bai F, Davidson JS. Analysis of partially composite foam insulated concrete sandwich structures. Eng Struct 2015;91:197–209.
[10] Williams Portal N, Flansbjer M, Zandi K, Wlasak L, Malaga K. Bending behaviour of novel Textile Reinforced Concrete-foamed concrete (TRC-FC) sandwich elements. Compos Struct 2017;177:104–18.
[11] di Prisco M, Plizzari G, Vandewalle L. Fibre reinforced concrete: new design perspectives. Mater Struct 2009;42:1261–81. https://doi.org/10.1617/s11527-009-9529-4.
[12] Reinhardt HW, Parra-Montesinos GJ, Garrecht H, editors. HPFRCC-7: proceedings of the 7th RILEM workshop on high performance fiber reinforced cement composites. Fraunhofer IRB Verlag; 2015.
[13] Peled A, Bentur A, Mobasher B. Textile reinforced concrete. 1st ed. Boca Raton, USA: CRC Press; 2017. p. 1–473.
[14] Brameshuber W, editor. Textile reinforced concrete - state-of-the-art report of RILEM technical committee 201. RILEM Publications S.A.R.L; 2006.
[15] Mobasher B, Peled A, Pahilajani J. Distributed cracking and stiffness degradation in fabric-cement composites. Mater Struct 2006;39(3):317–31.
[16] Colombo IG, Magri A, Zani G, Colombo M, di Prisco M. Textile reinforced concrete: experimental investigation on design parameters. Mater Struct 2013;46(11):1933–51.
[17] Zani G, Rampini MC, Colombo M, di Prisco M. Fire behavior of sandwich panels for roofing applications. Key Eng Mater 2016;711:775–82.
[18] Angelotti A, Leva S, Zani G, Di Prisco M. Sustainability-oriented innovation of a multilayered cement-based roof element; 2018. American Concrete Institute, ACI Special Publication, 2018-June (SP 326).
[19] ISO 15630-1:2010. Steel for the reinforcement and prestressing of concrete – Test methods – Part 1: Reinforcing bars, wire rod and wire. International Organization for Standardization.
[20] Zani G. High performance cementitious composites for sustainable roofing panels PhD Thesis Politecnico di Milano; 2013
[21] Colombo IG, Colombo M, di Prisco M, Pouyaei F. Analytical and numerical prediction of the bending behaviour of textile reinforced concrete sandwich beams. J Build Eng 2018;17:183–95.
[22] EN 14651:2005. Test method for metallic fibered concrete - Measuring the flexural tensile strength (limit of proportionality (LOP), residual). Brussels: European Committee for Standardization.
[23] fib Model Code 2010, Vol. 1, bull. 65. International Federation for Structural Concrete; 2012.
[24] fib Model Code 2010, Vol. 2, bull. 66. International Federation for Structural Concrete; 2012.
[25] Ferrara L, Ozyurt N, di Prisco M. High mechanical performance of fibre reinforced cementitious composites: the role of "casting-flow induced" fibre orientation. Mater Struct 2011;44(1):109–28. https://doi.org/10.1617/s11527-010-9613-9.
[26] EN 12390-3:2009. Testing hardened concrete - Part 3: Compressive strength of test specimens. Brussels: European Committee for Standardization.

[27] Butler M, Mechtcherine V, Hempel S. Durability of textile reinforced concrete made with AR glass fibre: effect of the matrix composition. Mater Struct 2010;43(10):1351–68.

[28] Micelli F, Aiello MA. Residual tensile strength of dry and impregnated reinforcement fibres after exposure to alkaline environments. Compos B 2019;159:490–501.

[29] RILEM Technical Committee 232-TDT (Wolfgang Brameshuber). Mater Struct 2016;49(12):4923–4927. < https://doi.org/10.1617/s11527-016-0839-z > .

[30] Bielak J, Li Y, Hegger J, Chudoba R. Numerical and experimental characterization of anchorage length for textile reinforced concrete. RILEM Bookseries 2018;15:409–17.

[31] Bazant ZP, Oh BH. Crack band theory for fracture of concrete. Mater Struct 1983;16(93):155–77.

[32] di Prisco M, Colombo M, Colombo IG. The role of the structural characteristic length in FRC structures. In: Saouma V, Bolander J, Landis E, editors. Proceedings of the 9th international conference on fracture mechanics of concrete and concrete structures FraMCoS-9. 2016.

[33] EN1990. Eurocode - basis of structural design. European Committee for Standardisation; 2002.